Design of a multi-analyte resonant photonic platform for label-free biosensing

To cite this article before publication: Chen Chen *et al* 2019 *Nanotechnology* in press https://doi.org/10.1088/1361-6528/ab0771

IOP Publishing Journal Title
Journal **XX** (XXXX) XXXXXX https://doi.org/XXXX/XXXX

Design of a multi-analyte resonant photonic platform for label-free biosensing

Chen Chen[1], Xun Hou[1] and Jinhai Si[1]

[1]The Key Laboratory for Physical Electronics and Devices of the Ministry of Education and the Shaanxi Key aboratory of Information Photonic Technique, School of Electronics and Information Engineering, Xi'an Jiaotong University Xi'an, China
E-mail:jinhaisi@ mail.xjtu.edu.cn
Received xxxxxx
Accepted for publication xxxxxx
Published xxxxxx

Abstract

We have designed a multi-analyte biosensing platform based on a hybrid whispering gallery mode resonator to detect protein biomarkers, e.g. those allowing the early diagnosis of Alzheimer's disease. Our proposed biosensor dependent on the hybrid mode naturally extends the capabilities of both plasmonic sensor and photonic sensor and thus performs better interrogation sensitivity. A multi-resonance of the hybrid mode could occur and the field intensity achieved its maximum value, thereby enabling a very strong light-matter interaction. The detection limit for bulk sensing reached a value of 2×10^{-5} RIU and that for surface sensing was at 0.6 pg/mm^2. Our novel configuration has an advantage over the conventional plasmonic-waveguide resonator with a similar cavity size (Q-factor < 500) because a wide range of spectral measurements (56 nm) and a high Q-factor (1300) could be achieved simultaneously. Thus, large refractive index shifts in the medium could be detected with high sensitivity. This biosensor, with a footprint of 625 μm^2 for each resonator, is a good candidate for integration into lab-on-chip microsystems for large-scale screening of a wide range of protein biomarkers in high risk of developing disease.

Keywords: Multi-analyte biosensing, hybrid WGM resonator, multi-resonance, Alzheimer's disease

1. Introduction

Alzheimer's disease (AD) is an age-dependent neurodegenerative disease that causes progressive cognitive impairment and memory deficits [1]. It is characterized by the deposition of extracellular amyloid-β (Aβ) peptide into amyloid plaques and the formation of intercellular neurofibrillary tangles that result in the collapse of microtubules[1]. A range of Aβ peptides from 40 to 43 amino acids can be derived from the successive cleavage of the amyloid precursor protein (APP) by γ-secretase [2]. Amyloid-β peptide 1-42 ($A\beta_{1-42}$) has been mainly observed in the brains of patients with AD in several different forms. These self-aggregated species range from a low molecular weight oligomer $A\beta_{1-42}$ (LMW $A\beta_{1-42}$) to a high molecular weight oligomer $A\beta_{1-42}$ (HWM $A\beta_{1-42}$), all of which contribute substantially to neurotoxicity and synapse impairment in AD [2]. Neurotoxic effects were observed when different species of $A\beta_{1-42}$ interacted with the extracellular D1D2 domain of the leukocyte immunoglobulin-like receptor B2 (ED1D2L) receptor [3]. Accordingly, three $A\beta_{1-42}$ species, namely monomeric (mono) $A\beta_{1-42}$, LMW $A\beta_{1-42}$, and HWM $A\beta_{1-42}$, can be used as biomarkers to diagnose and monitor the progression of AD. Thus, the demand for multi-analyte biosensing microsystems is large and still growing.

Whispering gallery mode (WGM) resonators feature multi-analyte detection capabilities, stability in aqueous environments, low cost and footprint that make them promising building blocks of the above-mentioned microsystems [4]-[5]. The quality factor (Q-factor), dependent on the cavity material and geometry, is widely used to evaluate WGM resonances. The radius of the resonator and its resulting Q-factor play an essential role in determining the magnitude of the resonance shift and the resultant biosensing capability. Typically, a larger cavity possesses a higher Q-factor. A smaller cavity presents a lower Q-factor but a larger resonance shift. To generate a multi-analyte microsystem, the cavities need to be very small. However, the Q-factor will be decreased. Thus, the trade-off between Q-factor and resonance shift should be considered based on the specific application of interest. Another quality, the full-width at half-maximum (FWHM), depends on the total losses in the cavity. Normally, the resonance shift ($\Delta\lambda_{res}$) cannot be observed unless it is comparable to or larger

than the FWHM [6]. Resonance shifts are required to be large enough so that the background noise can be effectively discriminated from the signal. An acceptable ratio of signal-to-noise requires the $\Delta\lambda_{res}$ to be in the order of 1/1000 to 1/100 of the FWHM. By extracting the sensitivity and FWHM values of a biosensor, one can evaluate its performance directly in terms of the LOD. Here, we assume the minimum detectable resonance shift as $\Delta\lambda_{min}$=1/200 × FWHM. Since the FWHM of the resonance wavelength is 1 nm, the resolution of the spectrum interrogation system should be 5 pm, which is readily available in our high-quality spectral interrogation system.

For conventional WGMs, however, only the evanescent tails of the resonant mode penetrate into the carrier fluid, resulting in modest sensitivity (below 200 RIU^{-1}) [4]. The introduction of localized surface plasmon (LSP) nanostructures in close proximity to dielectric WGM resonators offers unprecedented sensitivity in the detection of very low concentrations of target molecules [7,8]. The WGMs provide a resonance mode profile, the key feature of which is the sensing of perturbations in the ambient medium. Meanwhile, the electromagnetic field is greatly enhanced by the plasmonic component, giving rise to high sensitivity. Two of the proposed configurations for bulk sensing are: 1) a microring with nanostripes or nanodisks along the circumference [9,10] and 2) a microring (or micro-disk) in a metal–dielectric slot configuration [11]. Plasmonic resonance modes are intrinsically surface waves with longer evanescent tails more accessible to the analyte. Accordingly, the sensitivities of plasmonic resonance modes reach up to 1000 nm/RIU^{-1} for bulk sensing, which is one order of magnitude higher than the sensitivity value of pure dielectric resonators. Nevertheless, the main reason behind the adoption of LSP nanostructures lies in the detection of single objects. The dimensions of the nanostructure hot-spots (LSP resonances characterized by a strong field enhancement and confinement) are comparable to that of the target particles, which promotes these LSP nanoparticles as good candidates for single-object detection. Various configurations of microspheres and microtoroids with metallic nanoparticles, such as gold nanorods and gold nano-triangles, have demonstrated great promise in the detection of single particles and molecules [8,12]. However, the main challenge is the WGM damping in the metal. Consequently, the amount and distribution of LSP nanoparticles, which depend on the morphology of the resonator, have to be considered carefully.

Here, we report the design of a biosensing platform with a hybrid WGM resonator as the essential building block. Three resonators with different dimensions were evanescently coupled to the same bus waveguide, thus facilitating multi-analyte detection. Wavelength interrogation is taken in the measurement. Several resonance dips corresponding to the three microrings were presented at different positions in the output spectrum. Our proposed biosensor dependent on the hybrid mode, naturally extends the capabilities of both plasmonic sensor and photonic sensor and thus performs better interrogation sensitivity. The surface plasmon mode is excited by part of incident light on the metal-solution interface and localized in the nano-slot. SP modes with p-polarization are inspired on the surface metal films which are located on the side and top surfaces of the bus waveguide. Thus, dual polarization is supported in the whole structure. By addressing the structure with dual polarization, the optogeometrical properties (density and thickness) of protein layers have been determined without ambiguity. In the simulation work, we use commercial finite-element package FEMLab from COMSOL Multiphysics.

2. Design of the hybrid WGM platform

2.1 Architecture of the hybrid WGM resonator

Figure 1(a) shows the three-dimensional (3D) schematic structure of the proposed biosensing platform, composed of three hybrid WGM resonators with different microring radii. Each hybrid WGM resonator consisted of one outer ring coupled to the bus waveguide and one inner ring coupled to the outer ring. To generate the SP mode, two silver films were positioned very close to the top and side wall of the straight waveguide, which naturally formed a nano-slot with a reverse L shape. The bus waveguide and the microrings were made of silicon nitride (Si_3N_4), which provides lower loss and higher confinement in the near-infrared spectrum [13]. A Cytop polymer with a refractive index very similar to pure water was used to cover the entire structure in order to prevent external disturbances [14]. The sensing window for each resonator was etched into the top cladding to expose the surface of the microring and waveguide to the carrier fluid (index n_s) containing the target analyte. Inside each sensing window, biolayer was formed on the surface of the straight waveguide and the dual-microring resonator. The proposed structure was constructed with silicon dioxide (SiO_2) as the buffer. The cross-sectional view of the hybrid WGM resonator with geometrical dimensions is presented in Fig. 1(b). The straight waveguide had a width of w_{si3N4} = 0.5 μm and a height of h_{si3N4} = 0.73 μm. As measured from the inner edge, the radius of the outer ring was defined as r_{outer} and radius of the inner ring was r_{inner}. The widths of the outer ring and inner ring were expressed as b_{outer} and b_{inner}, respectively. For each WGM resonator, the gap between the straight waveguide and the outer ring (waveguide-ring) was g_1 = 100 nm and that between the outer and inner ring (ring-ring) was g_2 = 60 nm. The width of the silver film (w_{Ag}) was 1.56 μm, its height (h_{Ag}) was 1.79 μm, and its length was 2 μm. The silica buffer was 1 μm in thickness. The dimension of the slot between the metal films and the bus waveguide was denoted as w_{slot}. For all of the variables listed above, the

corresponding geometrical parameters of each resonator were set to: r_{outer1} = 11 μm, b_{outer1} = 0.48 μm, r_{inner1} = 4 μm, b_{inner1} = 0.75 μm, r_{outer2} = 14 μm, b_{outer2} = 0.46 μm, r_{inner2} = 4.15 μm, b_{inner2} = 0.51 μm, r_{outer3} = 10.8 μm, b_{outer3} = 0.48 μm, r_{inner3} = 4.3 μm, b_{inner3} = 0.52 μm, and w_{slot} = 60 nm, where the arabic numerals 1, 2, and 3 in subscript represent the three resonators. Our biosensor, with a footprint of 625 μm^2 for each resonator, is potential to be integrated into a lab-on-chip microsystem. In this simulation study, the refractive indices of silicon nitride and silica were calculated according to the literature [15,16]. The permittivity of silver was determined using the Drude-Sommerfeld model [17]. We take 1.3μm as operation wavelength since the optical absorption of water is smaller at a wavelength of 1.3 μm than at a 1.55 μm wavelength [18]. Materials with refractive indices in composition of biosensing platform are listed in table1. In Fig. 1(c), it is shown that a hybrid wave circulating around the resonator with strong intensity.

Table1. The materials with refractive indices in composition of biosensing platform are listed below.

Material	Refractive Index (RI)
Si_3N_4	2.0034
SiO_2	1.4469
Ag	0.10509+9.4986i
Cytop	1.334

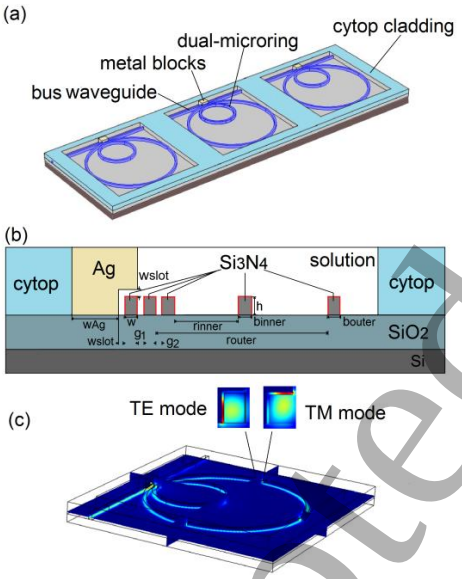

Fig. 1 (a) 3D schematic structure of proposed biosensing platform comprising of three hybrid WGM resonators. (b) Cross-sectional view of the hybrid WGM resonator with dimensions labeled. (c) The distribution of the electromagnetic field of the hybrid mode for one resonator.

2.2 Theory underlying the hybrid plasmonic resonator

In a dielectric WGM resonator, only the evanescent tails of the resonant mode penetrate into the carrier fluid, resulting in modest sensitivity (below 200 RIU^{-1}). To improve the scenario, two silver films were introduced in close proximity to the bus waveguide in order to excite SP mode. In addition, the location of the metal films overlapped in the longitudinal direction with the waveguide-ring coupling region and the ring-ring coupling region to promote multi-resonance in the whole structure. The incident wave, which can be launched from an infrared laser, was propagated through the bus waveguide. In the coupling region, a portion of incident wave excited the SP mode propagating parallel along the metal surface and localized in the gap region, another part of which is transferred into the dual microring and further inspired the WGM around the double ring. It has been confirmed that strong energy is stored in the nano-slot with low-permittivity dielectric [19]. The reason arises from the discontinuity of electric filed at the material interfaces, which results in a stronger normal electric field components (E_x corresponding to the TE mode and E_y corresponding to the TM mode of the bus waveguide) in the slot with lower dielectric constant. The dielectric discontinuity at the waveguide-solution interface produces a polarization charge which interacts with the plasma oscillation on the metal-solution interface. In other words, the nano-slot has an effective optical capacitance. By adjusting the nano-slot, we can control the hybridization of the SP mode and WGM. When the nano-slot is 60nm in width, the hybrid mode has equal SP and WGM characteristics, indicating that polarization charge and plasma oscillation move in phase and maximize the effective optical capacitance of the waveguide. When the phase velocity of the SP mode and WGM matched, multi-resonance occurred in the entire structure. The hybrid field achieved its maximum intensity and was well distributed into the device. It has been previously demonstrated that the addition of a metal block can reduce the power radiation leakage and thus make the highly curved microring available [11]. Due to the hybrid mode, little energy is distributed into the metal and thus the Q-factor is larger than that of conventional SP microresonators. The biosensor dependent on the hybrid mode, naturally extends the capabilities of both plasmonic sensor and photonic sensor, thereby making the bulk sensing and single-object tracing available.

A high-performance biosensor is required to have high resolution in order to trace tiny changes in the ambient index. High sensitivity and a high Q-factor are preferred. At the same time, it is also desirable to have a large spectral range of measurement (free spectral range; FSR) so that large index shifts in the medium can be detected. For a conventional resonator, the values of FSR and Q-factor are mainly determined by the microring radius; the FSR increases with decreasing microring radius and the Q-factor increases with increasing microring radius. Therefore, it is a challenge to simultaneously achieve a high Q-factor and a wide range of measurement in a single-ring resonator. A dual-microring configuration (an inner ring coupled with an outer ring) has

been reported to solve this problem [20]. In our work, this double-ring structure was modified by adjusting the location of the inner ring such that the ring-ring coupling region overlapped with the waveguide-ring coupling region and the gap between metal film and bus waveguide. As a result, the occurrence of multi-resonance allowed the effective mode index of the hybrid mode to achieve its maximum value and the FSR was expanded. Moreover, the hybrid mode probably sharpened the resonance peak, resulting in a high Q-factor. Taken together, we confirmed that the dual-microring configuration was capable of simultaneously improving the FSR and the Q-factor. The extra advantage of the double-ring configuration was that it kept the footprint of the cavity to a minimum, which allows this design to be integrated into a lab-on-chip microsystem.

2.3 Performance analysis

We conducted a performance analysis of the hybrid WGM resonator (third resonator as the target) via numerical calculation. Firstly, we focused on the influence of the slot dimension on the bulk-sensing performance. The width of the nano-slot (w_{slot}) ranged from 40 - 120 nm (step = 20 nm). The effective mode index of the hybrid mode, dependent on the wavelength variation, was investigated (Fig. 2). The corresponding electromagnetic field distributions of hybrid mode are presented in Fig. 3. Narrower slots provided higher effective mode indices. In Fig. 3, the intensity of the SP mode became greater when the slot width decreased. Specifically, when the slot width was 40 nm, the SP mode was the dominant recipient of excitation by the incident wave energy and little energy was transferred into the microring resonator. This indicated that the metal films were capable of attracting the optical power to the gap region, in which the field is highly confined. With the 40 nm slot width, the effective mode index was large, yet less of the energy was coupled into the resonator. When the slot width was larger than 80 nm, most of the incident light was transferred into the resonator while less light excited the SP mode in the slot. At these large slot widths, the hybrid WGM resonator deteriorated to a pure dielectric WGM resonator. Therefore, a nano-slot that was too narrow or too wide perturbed the entire configuration out of multi-resonance. Only when the slot width was 60 nm did the hybrid mode has equal SP mode and WGM characteristics and multi-resonance occur, thus obtaining the maximum value of the hybrid mode index with the hybrid field well-distributed over the entire structure.

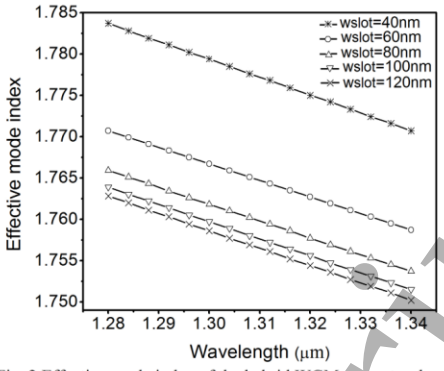

Fig. 2 Effective mode index of the hybrid WGM resonator depedent on the nano-slot dimension (40-120nm).

Sensitivity (S) refers to the ability to detect a target analyte in the carrier fluid. For bulk sensing, sensitivity was calculated by altering the bulk index (n_s) by a small amount for different slot widths, since the bulk index ranges from 1.33 to 1.37 for most affinity-sensing schemes (Fig. 4a). Sensitivity generally reflected the strength of the light-matter interaction; a strong field is able to provide a high value of sensitivity. When the slot width was 40 nm, maximum sensitivity was achieved. However, as shown in the hybrid field distribution in Fig. 3, less of the optical field was coupled to the resonator. The sensitivity arose from the strongly confined SP mode. With increased slot width, much more of the optical filed was transferred into the resonator. When the slot width was 60 nm, the hybrid field intensity achieved its maximum value and accordingly the sensitivity was greatly improved. When the slot width was larger than 80 nm, little SP mode was generated on the surface of the metal films and the hybrid WGM resonator degenerated into a dielectric resonator. The sensitivity was also greatly reduced.

Assuming the critical coupling condition, the change in the Q-factor with different slot widths was calculated and is plotted in Fig. 4b. The Q-factor ($>10^3$) of our design was smaller than that of a dielectric resonator (whose experimental value is above 10^4). The reason for this lies in the scattering loss associated with a metallic SP mode and the bending loss associated with the small-size cavity. However, our Q-factor was larger than that of microring resonators composed solely of plasmonic waveguides with a similar cavity size (Q-factor less than 500) [21].

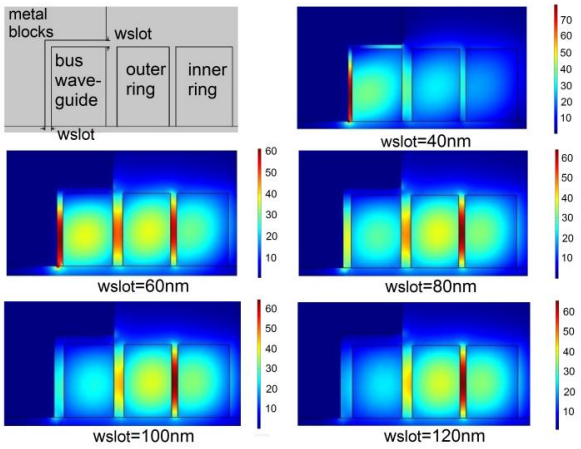

Fig. 3 The field distribution of hybrid mode corresponding to different nano-slot widths.

The limit of detection (LOD), defined as the smallest amount of analyte that can be detected by the sensor system, depends on both the sensitivity and the profile of the resonance spectrum (in other words, the FWHM of the resonance spectrum). To achieve a low value of LOD, a high Q-factor is necessary. From the data in Fig. 4b and 4c, we can conclude that a high Q-factor is required to effectively reduce the LOD. In our device, the LOD can be brought down to 2×10^{-5} RIU with a slot width of 60 nm (Fig. 4c).

Figure of merit (FOM) is also extensively utilized to characterize the performance of different configurations. FOM takes the sharpness of the resonance into consideration through the FWHM of the peak [22,23]. The change in FOM with different slot width was calculated and is plotted in Fig. 4d. For bulk sensing, performance increased as the slot width decreased. The maximum achievable FOM was 240, which occurred at the slot width of 60nm. Taking into consideration of all the essential parameters above, a slot width of 60nm was adopted into the final design of our hybrid resonator.

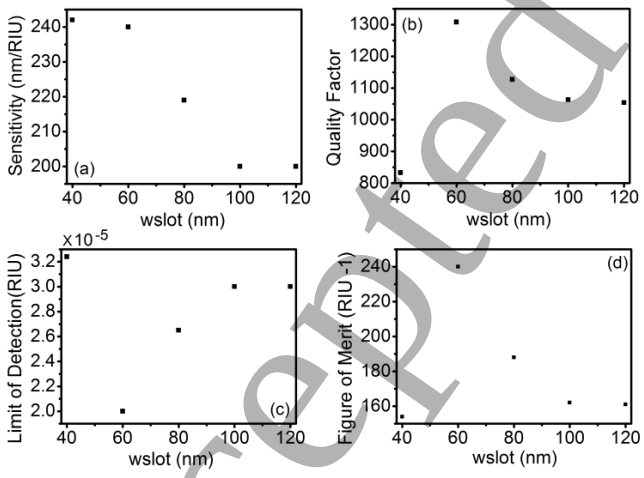

Fig. 4 The influence of nano-slot dimension on the (a) bulk sensitivity, (b) Q-factor, (c) the LOD, and (d) the FOM.

To emphasize the significance of the double-ring in the complex configuration, we investigated the resonance spectrum of different configurations and analyzed the values of FSR, Q-factor, and effective mode index. The single-ring structure perturbed the complete configuration out of multi-resonance, as observed in Fig. 5 with the resonance dips shifting from λ_{res} = 1.308 μm for the dual-microring to λ_{res} = 1.307 μm for the outer ring and λ_{res} = 1.316 μm for the inner ring. In Fig. 5a, we can see that our chosen structure design (i.e., dual-microring with metal films) resulted in the best performance, as indicated by the large FSR and high Q-factor. To explore the effect of the double-ring configuration, we investigated the performance of the structure with only outer ring or only inner ring resonators, the resonance spectrums of which are plotted in Fig. 5b and 5c. The FSR of the dual-microring resonator (FSR = 56 nm) was superior to that of both the single-ring resonators (FSR = 23 nm for the outer-ring resonator and FSR = 27 nm for the inner-ring resonator). In fact, the FSR of the dual-microring was twice as large as that of the inner-ring configuration. For a single-ring resonator, FSR is dependent on the size of the resonator and the effective mode index of the WGM. Large resonators have a dense transmission spectrum, while small ones have widely spaced resonance dips. The effective radius of a dual-microring is not the sum of the radius of its inner ring and outer ring. On the contrary, the effective radius is probably smaller than the radius of the inner ring, thus resulting in broadly spaced resonance dips. Due to the multi-resonance in the dual-microring configuration, the effective mode index of the hybrid mode achieved the maximum value and FSR was expanded.

The Q-factor of a single-ring resonator is affected by the resonance spectrum profile and a sharp resonance dip is normally characterized by a high Q-factor. The FWHM was used to describe the shape of the resonance dips. Comparing Fig. 5b and 5c, we can see that the FWHM of the inner-ring resonator is larger than that of the outer-ring resonator. Since a greater curvature of the cavity causes greater bending loss, the resonance peak is correspondingly broadened. Consequently, the Q-factor of the outer-ring resonator is higher than that of the inner-ring resonator. However, the Q-factor of the dual-microring configuration (Q = 1308) is twice as high as that of the single outer-ring resonator (Q = 653.5) and even more improved over that of the inner-ring resonator (Q = 376). The hybrid mode probably sharpens the resonance peak, and as a result, a high Q-factor is achieved.

We also explored how the metal affects the performance of the device. We assessed the effective mode index of the hybrid wave in the architecture with and without silver films. The effective mode index is directly related to the field intensity, which determines the strength of the interaction between light and matter. Compared with a dielectric WGM resonator, the resonator with metal films had a high effective mode index value (Fig. 5d). Plasmon modes are intrinsically surface wave with longer evanescent tails more accessible to the analyte. The location of the metal films overlapped in the

longitudinal direction with the waveguide-ring coupling region and ring-ring coupling region, thereby promoting multi-resonance in the whole structure. The effective mode index of the hybrid mode was substantially enhanced. Consequently, the interaction between the electromagnetic field and the target analyte was substantially strengthened.

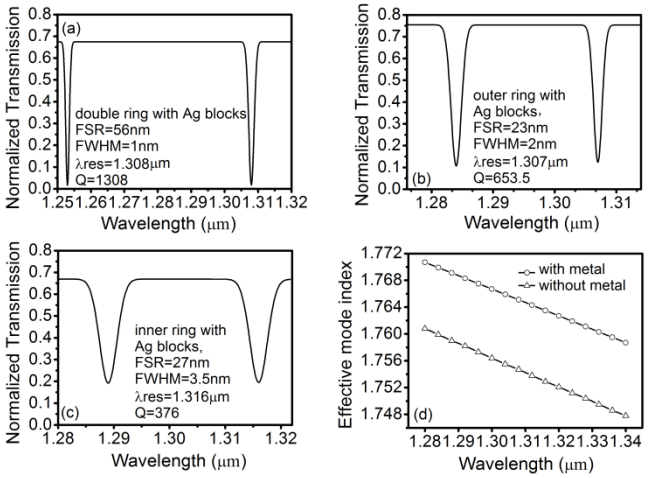

Fig. 5 Resonance spectrums of (a) complete configuration with dual-microring and metal blocks, (b) configuration with outer ring and metal blocks, and (c) configuration with inner ring and metal blocks. (d) Effective mode index depedent on the metal blocks.

The coupling coefficient κ, characterizes how much of the optical energy passing from a bus waveguide to a bent one, when it comes to a microring resonator. In the dual-microring resonator, two couplers were presented, one of which consisted of a bus waveguide and an outer ring and the other of which consisted of a double ring. The coupling coefficients (κ1 and κ2) between modes propagating in the two couplers are dependent on the gap distances in the waveguide-ring (g_1) and the ring-ring (g_2) couplers (Fig. 6a and 6b). The κ dependent on g for the waveguide-ring and ring-ring couplers, respectively, were fitted by the following exponential equations: $\kappa 1 = K_1 \exp(K_2 \times g_1)$ and $\kappa 2 = K_3 \exp(K_4 \times g_2)$, where $K_1 = 0.9976$, $K_2 = -0.0045$ nm^{-1}, $K_3 = 0.9951$, and $K_4 = -0.012$ nm^{-1} are fitting coefficients based on the geometrical and optical properties of the couplers. As expected, the coupling coefficient decreased as the gap distance increased for each coupler. This indicated that small gaps are necessary to achieve a high coupling efficiency.

The influence of the coupling coefficient on the optical transmission was taken into consideration as well. The transmission spectrums with different coupling coefficients are presented in Fig. 6c and 6d. Different values of κ characterized specific resonance spectrum profiles. This indicated that the coupling coefficient had a direct effect on the shape of the resonance dip, thereby affecting the Q-factor. It was shown that a low value for FWHM corresponding to a small κ. Resonance dips became sharper as the value of κ decreased. Compared with κ2, the coefficient κ1 had a stronger influence on the spectrum; the spectrum intensively deteriorated when the κ1 was less than 0.44, indicating that less energy was transferred into the dual-microring and the coupling efficiency was markedly reduced. When the gap between the waveguide and the resonator exceeds a certain value, the optical wave is hardly coupled into the resonator and there is no WGM in the complete structure. Although κ2 has less of an effect on the dip intensity, it is worth noting that a κ2 less than 0.3 shifted the resonance wavelength to 1.307 μm, which corresponds to the resonance wavelength of a pure outer-ring configuration (Fig. 5b). This indicated that a double-ring resonator deteriorated to a single-ring resonator when the gap distance of the ring-ring coupler was too large. Thus, we can optimize the hybrid WGM resonator by tuning the gaps of the ring-waveguide and ring-ring couplers. In this study, we chose the values κ1 = 0.64 corresponding to g_1 = 100 nm and κ2 = 0.48 corresponding to g_2 = 60 nm when designing our device.

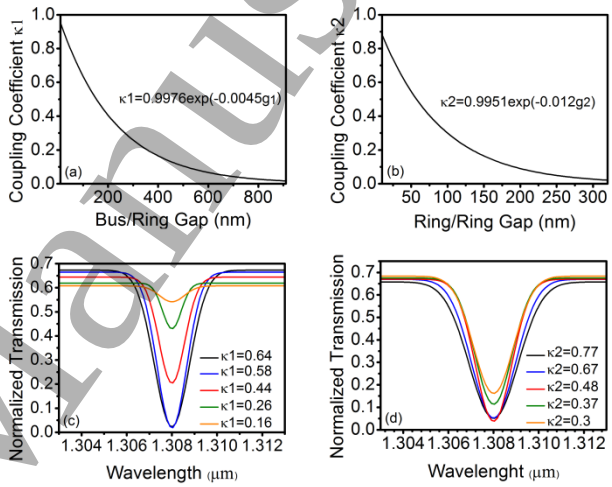

Fig. 6 Coupling coefficient as a function of (a) the waveguide-ring gap, and (b) the ring-ring gap. Transmission spectrums as a function of (c) the coupling coefficient κ1 and (d) the coupling coefficient κ2.

3. Multi-analyte detection based on the hybrid WGM platform

The resonator surface was modified with a BS_3 linker, a homo-bifunctional crosslinker that can provide amine reactive functionalities in advance. All of the three $A\beta_{1-42}$ molecules specifically recognize and interact with the ED1D2L receptors in an aqueous solution. The binding event consisted of several distinct steps [2]: (1) Tris buffer flowing over the BS_3-functionalized resonator surface for initial calibration, (2) immobilization of the ED1D2L receptor to the resonator surface via covalent binding to the BS_3 linker, (3) introduction of bovine serum albumin (BSA) and ethanolamine to block the remaining amine and prevent non-specific binding, and (4) introduction of $A\beta_{1-42}$ molecules into the three resonators (HMW $A\beta_{1-42}$ into the first resonator, LMW $A\beta_{1-42}$ into the second resonator and mono $A\beta_{1-42}$ into the third resonator). The bulk index of Tris buffer

was assumed to be 1.335. The thickness a and index n_l of the biolayer were obtained from typical literature data corresponding to the analyte concentration of 100 nM [2]. All data including n_s, n_l, and a are listed in table 2.

Table 2 Biological materials introduced into the hybrid WGM platform.

	Material	Bulk index n_s	Biolayer index n_l	Biolayer thickness a (nm)
Three resonators	Tris buffer	1.335	0	0
Three resonators	ED1D2L receptor	1.335	1.455	2.08
First resonator	HMW $A\beta_{1-42}$	1.335	1.36	9.58
Second resonator	LMW $A\beta_{1-42}$	1.335	1.409	2.83
Third resonator	mono $A\beta_{1-42}$	1.335	1.403	3.08

The output spectrum characterizing the complete biological event is presented in Fig. 7. Three series of resonance dips from 1.265 μm to 1.32 μm, each corresponding to one resonator, are presented. For each resonator, the monitored interference patterns were red-shifted with increased biolayer thickness. The resonance wavelengths, relevant to the three $A\beta_{1-42}$ species, are clearly observed in the spectrum. By tracking the resonance dip, the microsystem was capable of estimating the concentration of three target biomarkers in the biological fluid. The minimum resonance shift ($\Delta\lambda_{res}$ = 1 nm) was caused by a biolayer thickness change of 1 nm (δa = 1nm). Sensitivity and LOD are evaluated during the binding event. As mentioned earlier, bulk sensing is simulated by perturbing the bulk index n_s by a small amount. For surface sensing, biolayer formation is modeled as the growth of dielectric film with thickness from 1.5 nm to 10.5 nm and refractive index n_l = 1.45. The sensitivity of the biosensing platform can reach 240 nm/RIU for bulk sensing and 1.2 nm/nm for surface sensing. The LOD can be expressed in two main ways: for bulk sensing, it can be defined as $\Delta n_{s,min}$ (RIU) [23] and for surface sensing, it can be expressed as surface mass density Γ_{min} (pg/mm^2) [23]. The bulk detection limit was 2 × 10^{-5} RIU. The LOD based on absorbed molecules on the surface reached a value of 0.6 pg/mm^2.

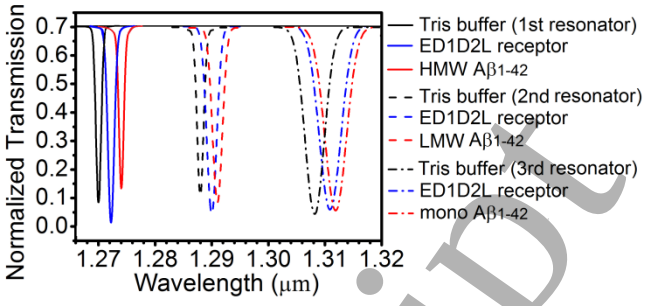

Fig. 7 Output spectrum of the biosensing platform. Three series of resonance dips from 1.265μm to 1.32μm, each corresponding to one resonator.

The fabrication can start from deposition of a 730 nm Si_3N_4 thin film on a 1 μm SiO_2 buffer using plasmon enhanced chemical vapor deposition (PECVD). The wafer is spin-coated with PMMA8 resist with 750 nm thick followed by electron beam lithography (EBL) for patterning the silver film. The extra Si_3N_4 material is removed by reactive ion etching (RIE) and silver film is formed via magnetron sputtering. The extra Ag film and resist are cleaned with acetone and isopropanol solution. Silver film located on the sidewall of bus waveguide is subsequently produced. After that, resist HSQ is spin-coated and waveguide and double ring patterns are constructed by means of EBL and RIE. The significant issue is another Ag film which located very close to the upper surface of bus waveguide (the slot width is 60 nm). Polymide reagent is taken to smooth the pattern surface so as to make the nano-slot between the upper surface of the bus waveguide and Ag film. The top silver pattern is constructed by EBL and RIE. The Ag film is generated by magnetron sputtering. Remove the residual resist and the whole configuration is finally produced. The designed structure is coated with Cytop layer later. The sensing window for each resonator was etched into the top cladding to expose the surface of the microring and waveguide to the carrier fluid containing the target analyte.

4. Conclusions

We designed a multi-analyte biosensing platform based on the hybrid WGM resonator. The sensor focused on measuring the concentration of protein biomarkers. The sensor was able to simultaneously improve the FSR and the Q-factor. Our proposed biosensor dependent on the hybrid mode naturally extends the capabilities of both plasmonic sensor and photonic sensor and thus performs better interrogation sensitivity. The LOD of the proposed microsystem was 2 × 10^{-5} RIU for bulk sensing and 0.6 pg/mm^2 for surface sensing. The output spectrum successfully detected three biomarkers with concentrations of 100 nM. Our device, with a footprint of 625 μm^2 for each resonator, has the potential to be integrated into lab-on-chip microsystems.

Acknowledgements

This work was supported in part by the National Natural Science Foundation of China (NSFC) under Grant Nos. 61690221 and 61427816 and in part by Collaborative Innovation Center of Suzhou Nano Science and Technology.

Appendix

The design of the biosensing platform depends on the transfer matrix method (TMM) [24] which is shown in Fig. 8a. When an incident light with amplitude a^{I} arrives at the coupling region, one portion of which excited the SP mode on the metal-solution interface, another of which transferred into the dual-microring resonator and excited the WGM. The amplitude of SP mode is expressed as $a_s = \kappa_s a^{\mathrm{I}}$, where κ_s is the coupling coefficient dependent on the distance g_s, the dimension of silver film, and the dielectric index in the gap region. The amplitude of WGM is expressed as $a_1 = \kappa_{\mathrm{i}} a^{\mathrm{I}}$, in which κ_i is the coupling coefficient determined by various factors, such as the gap of waveguide-ring and that of double ring, diameters of dual-microring, cross-section area of microrings, materials of waveguide and double ring, and coupling coefficient κ_s. For the lossless coupling, $\kappa_{\mathrm{i}}^2 + \kappa_{\mathrm{s}}^2 = 1$, $\kappa_{\mathrm{i}}^2 = \kappa_1^2 + t_1^2$, and $\kappa_1^2 = \kappa_2^2 + t_2^2$. With the help of the transfer matrix method (TMM), in the coupling regions, we have

$$b_1 = t_1 a_1 + j\kappa_1 a_2 \quad (1\text{-}1)$$

$$b_2 = j\kappa_1 a_1 + t_1 a_2 \quad (1\text{-}2)$$

$$b_2 = t_2 a_2 + j\kappa_2 a_3 \quad (1\text{-}3)$$

$$b_3 = j\kappa_2 a_2 + t_2 a_3 \quad (1\text{-}4)$$

where a_1, a_2, a_3 are input amplitudes, b_1, b_2, and b_3 are output amplitudes, and t_1 and t_2 are the transmission coefficients. Transmission equations from one coupling region to another can be written as

$$a_2 = b_2 e^{-\alpha_1 L_1} e^{-j\beta_1 L_1} \quad (2\text{-}1)$$

$$a_3 = b_3 e^{-\alpha_2 L_2} e^{-j\beta_2 L_2} \quad (2\text{-}2)$$

$$b_s = a_s e^{-\alpha_{SP} L_{ag}} e^{-j\beta_{SP} L_{ag}} \quad (2\text{-}3)$$

where $\alpha_i (i = 1, 2)$ and $\beta_i (i = 1, 2)$ are attenuation and phase constant of outer ring (i = 1) and inner ring (i = 2) respectively, and $\beta_i = 2\pi n_{eff\_i} / \lambda_0 \ (i = 1, 2)$ with $n_{eff\_i} (i = 1, 2)$ the effective mode indices of WGM in the outer ring (i = 1) or that of WGM in the inner ring (i = 2), is depending on the geometrical parameters of double ring, matrial refractive index and operation wavelength. The parameters α_{SP} and β_{SP} are the attenuation and phase constant of SP mode respectively, and $\beta_{sp} = 2\pi n_{eff\_s} / \lambda_0$ with n_{eff_s} the effective mode index of SP mode. The parameters L_1 and L_2 are the perimeters of outer ring and inner ring repsectively. L_{ag} is the length of the silver film. Equation (2-2) is rewritten as

$$b_3 = a_3 e^{\alpha_2 L_2} e^{j\beta_2 L_2} \quad (3)$$

Substitute eq. (3) into eq. (1-4), we can obtain

$$a_3 = \frac{j\kappa_2}{(e^{\alpha_2 L_2} e^{j\beta_2 L_2} - t_2)} a_2 \quad (4)$$

Substitute eq. (2-1) into eq. (4), we can obtain

$$a_3 = \frac{j\kappa_2}{(e^{\alpha_2 L_2} e^{j\beta_2 L_2} - t_2)} e^{-\alpha_1 L_1} e^{-j\beta_1 L_1} b_2 \quad (5)$$

Substitute eq. (5) into eq. (1-3), we can obtain

$$b_2 = \frac{t_2 a_2}{1 + \dfrac{\kappa_2^2 e^{-\alpha_1 L_1} e^{-j\beta_1 L_1}}{e^{\alpha_2 L_2} e^{j\beta_2 L_2} - t_2}} \quad (6)$$

Substitute eq. (6) into eq. (1-2), we can obtain

$$a_2 = j\kappa_1 \left[\frac{t_2}{1 + (\kappa_2^2 e^{-\alpha_1 L_1} e^{-j\beta_1 L_1}) / (e^{\alpha_2 L_2} e^{j\beta_2 L_2} - t_2)} - t_1 \right]^{-1} a_1 \quad (7)$$

Substitute eq. (7) into eq. (1-1), we can obtain

$$b_1 = \left\{ t_1 - \kappa_1^2 \left[\frac{t_2}{1 + (\kappa_2^2 e^{-\alpha_1 L_1} e^{-j\beta_1 L_1}) / (e^{\alpha_2 L_2} e^{j\beta_2 L_2} - t_2)} - t_1 \right]^{-1} \right\} a_1 \quad (8)$$

Since $b^{\mathrm{I}} = b_1 + b_s$

$$= \left\{ t_1 - \kappa_1^2 \left[\frac{t_2}{1 + (\kappa_2^2 e^{-\alpha_1 L_1} e^{-j\beta_1 L_1}) / (e^{\alpha_2 L_2} e^{j\beta_2 L_2} - t_2)} - t_1 \right]^{-1} \right\} \kappa_{\mathrm{i}} a^{\mathrm{I}} \quad (9)$$
$$+ \kappa_s a^{\mathrm{I}} e^{-\alpha_{sp} L_{ag}} e^{-j\beta_{sp} L_{ag}}$$

Set $T^{\mathrm{I}} = \dfrac{b^{\mathrm{I}}}{a^{\mathrm{I}}}$, we get

$$T^{\mathrm{I}} = \frac{b^{\mathrm{I}}}{a^{\mathrm{I}}} = \left\{ t_1 - \kappa_1^2 \left[\frac{t_2}{1 + (\kappa_2^2 e^{-\alpha_1 L_1} e^{-j\beta_1 L_1}) / (e^{\alpha_2 L_2} e^{j\beta_2 L_2} - t_2)} - t_1 \right]^{-1} \right\} \kappa_{\mathrm{i}} \quad (10)$$
$$+ \kappa_s e^{-\alpha_{SP} L_{ag}} e^{-j\beta_{SP} L_{ag}}$$

where T^{I} is the TMM of the Ith hybrid WGM resonator and is determined by various factors, such as geometerical parameters of double ring, refractive index of double ring, coupling coefficient, transmission coefficient and operation wavelength, etc.

Three WGM resonators work simutanously and each resonator has its individual resonance wavelength. Thus, the total transmission (Fig. 1b) can be expressed as

$$T_{ALL} = \frac{b^3}{a^1} = \frac{b^1}{a^1} \cdot \frac{a^2}{b^1} \cdot \frac{b^2}{a^2} \cdot \frac{a^3}{b^2} \cdot \frac{b^3}{a^3} = \prod_{\mathrm{I}=1}^{3} T^{\mathrm{I}} \quad (11)$$

We aim to get the geometrical parameters of the device which present three resonance wavelengths with predefined value (λ_{r1}, λ_{r2},, λ_{r3},). Thus, three series of resonance dips corresponding to resonance wavelengths are expected in the

output spectrum. By means of optimized design with multi-objective function, we can sovle the eq. (11) and get the geometrical parameters of our proposed structure. In this work, we used commercial finite-element package FEMLab from COMSOL Multiphysics. The mode analysis solver was used to find the hybrid mode with the effective mode index. In the simulation of 3D configuration, we took boundary mode analysis solver to get power outflow (time average) of the input port and the output port. By parametric sweep, we can solve the eq. (11) in the predefined resonance wavelengths thereby getting the optimized geometrical structure. The perfect matching layer and scattering boundary condition were given to mimic the necessary open boundary conditions and thus guarantee the accurate calculation. A convergence analysis is conducted to ensure the calculation results accurate. Convergence of the numerical solution indicates that the meshing, boundary conditions and associated calculation parameters were sound.

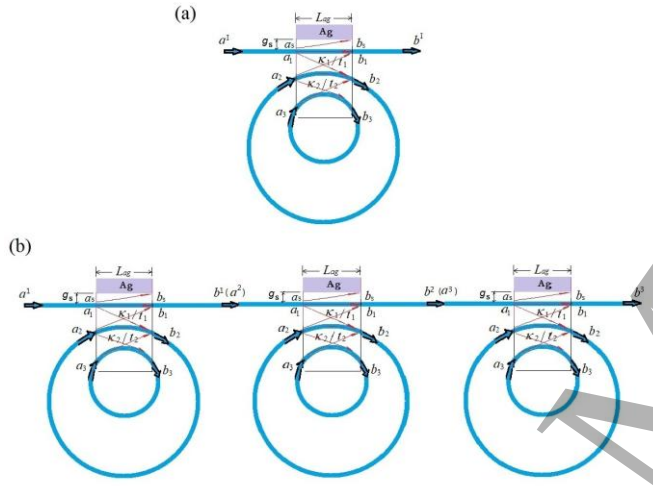

Fig. 8 Schematic of a single WGM resonator (a) and three WGM resonators in series (b) with parameters including input and output amplitudes, tranmission coefficients, coupling coefficients.

References

[1] Wyss-Coray, T. "Inflammation in Alzheimer disease: driving force, bystander or beneficial response? " *Nat. Med.*, vol 12, no.9, pp. 1005−1015, 2006.

[2] Hu T, Wang S, Chen C, Sun J and Yang X. "Real-Time Analysis of Binding Events between Different $A\beta_{1-42}$ Species and Human $Lilrb_2$ by Dual Polarization Interferometry," *Anal. Chem.*, vol. 89, no. 4, pp. 2606-2612, 2017.

[3] Benilova I, De Strooper B. "Promiscuous Alzheimer's Amyloid: Yet Another Partner," *Science*, vol. 341, no. 6152, pp. 1354-1355, 2013.

[4] Bozzola A, Perotto S and De Angelis F. "Hybrid plasmonic–photonic whispering gallery mode resonators for sensing: a critical review," *Analyst*, vol. 142, no. 6, pp. 883-898, 2017.

[5] Foreman MR, Swaim JD and Vollmer F. "Whispering gallery mode sensors," *Adv. Opt. Photonics*,vol. 7, no. 2, pp. 168-240, 2015.

[6] Vollmer F and Arnold S. "Whispering-gallery-mode biosensing: label free detection down to single molecules," *Nat. Methods*, vol. 5, no. 7, pp. 591-596, 2008.

[7] De Angelis F, Patrini M, Das M, Maksymov I, Galli M, Businaro L, Andreani LC and Di Fabrizio E. "A Hybrid Plasmonic-Photonic Nanodevice for Label-Free Detection of a Few Molecules," *Nano Lett.*, vol. 8, no. 8, pp. 2321–2327, 2008.

[8] Dantham VR, Holler S, Barbre C, Keng D, Kolchenko V and Arnold S. "Label-Free Detection of Single Protein Using a Nano plasmonic-Photonic Hybrid Microcavity," *Nano Lett.*, vol. 13, no. 7, pp. 3347-3351, 2013.

[9] Zhang M, Wu G and Chen D. "Silicon hybrid plasmonic microring resonator for sensing applications," *Appl. Opt.*, vol. 54, no. 23, pp. 7131-7134, 2015.

[10] Urbonas D, Balcytis A, Gabalis M, Vaskevicius K, Naujokaite G, Juodkazis S and Petruskevicius R. "Ultra-wide free spectral range, enhanced sensitivity, and removed mode splitting SOI optical ring resonator with dispersive metal nanodisks," *Opt. Lett.*, vol. 40, no. 13,pp. 2977-2980, 2015.

[11] Zhou L, Sun X, Li X and Chen J. "Miniature Microring Resonator Sensor Based on a Hybrid Plasmonic Waveguide," *Sensors*, vol. 11, no. 7, pp. 6856-6867, 2011.

[12] Nadgaran H, Garaei MA. "Enhancement of a whispering gallery mode microtoroid resonator by plasmonic triangular gold nanoprism for label-free biosensor applications," *J. Appl. Phys.*, vol. 20, no. 19, pp. 239-214, 2015.

[13] Gondarenko A, Levy JS and Lipson M. "High confinement micron-scale silicon nitride high Q ring resonator," *Opt. Express*, vol. 17, no. 14, pp. 11366-11370, 2009.

[14] http://www.bellexinternational.com/products/cytop/

[15] Luke K, Okawachi Y, Lamont MR, Gaeta AL, and Lipson M. "Broadband mid-infrared frequency comb generation in a Si_3N_4 microresonator," *Opt. Lett.*, vol. 40, no. 21, 4823-4826, 2015.

[16] Lide and David R. CRC Handbook of Chemistry and Physics, Internet Version (Taylor and Francis, Boca Raton, FL, 2007)

[17] Chen C, Hou X, and Si J. "Protein analysis by Mach-Zehnder interferometers with a hybrid plasmonic waveguide with nano-slots," *Opt. Express*, vol. 25, no. 25, 31294-31308, 2017.

[18] Dell'Olio F, Conteduca D, Ciminelli C, and Armenise MN. "New ultrasensitive resonant photonic platform for label-free biosensing," *Opt. Express*, vol. 23, no. 22, 28593-28604, 2015.

[19] Oulton RF, Sorger VJ, Bartal G, and Zhang X. "A Hybrid Plasmonic Waveguide for Subwavelength Confinement and Long Range Propagation," nat. photonics, vol. 2, 496-500, 2008

[20] Su B, Wang C, Kan Q and Chen H. "Compact Silicon-on-Insulator Dual-Microring Resonator Optimized for Sensing," *J. Lightwave Technol.*, vol. 29, no. 10, 1535-1541, 2011.

[21] Zangeneh-Nejad F andSafian R. "A Graphene-Based THz Ring Resonator for Label-Free Sensing," *IEEE Sens. J.*, vol. 16, no. 11, pp. 4338-4344, 2016.

[22] Sherry LJ, Chang SH, Schatz GC, Van Duyne RP, Wiley BJ and Y Xia. "Localized Surface Plasmon Resonance Spectroscopy of Single Silver Nanocubes," *Nano. Lett.*, vol. 5, no. 10, pp. 2034-2038, 2005.

[23] Gazzaz K and Berini P. "Theoretical biosensing performance of surface plasmon polariton Bragg gratings," *Appl. Opt.*, vol. 54, no. 7, pp. 1673-1680, 2015.

[24] Yariv A. "Universal relations for coupling of optical power between microresonators and dielectric waveguides," *electron lett.*, vol. 36, no. 4, pp. 321-322 , 2000.